Supporting Information

Reconciling Work Functions and Adsorption Enthalpies for Implicit Solvent: A Pt (111)/Water Interface Case Study

Gabriel Bramley[1], Manh-Thuong Nguyen[2], Vassiliki-Alexandra Glezakou[2], Roger Rousseau[2], Chris-Kriton Skylaris[1]

[1] School of Chemistry, University of Southampton, Southampton SO17 1BJ, UK

[2] Physical Sciences Division, Pacific Northern National Laboratory, Richland, WA 99352, USA

S1. Pt Vacuum Benchmarks

Ab initio methods provide a powerful computational tool to accurately simulate surface properties. Several benchmark studies[1-3] using the periodic supercell model have been conducted using a range of Density Functional Theory (DFT) methods. Such simulations are often done with the plane wave (PW) formalism for DFT calculations, which allows one to calculate charge density, energies and band structures through integration across the Brillouin zone (BZ).[4] Sampling techniques such as the Monkhorst-Pack scheme[5] allow for the efficient integration of the BZ via a summation of special **k**-points evenly distributed throughout the first Brillouin zone (1BZ).[5]

Typically, surface properties tend to be highly dependent on both the thickness of the slab and sampling of the 1BZ. It is therefore important to test for convergence by both sequentially increasing the number of layers of the surface slab and increasing the density of **k**-point sampling.

Using standard PW methods, Singh-Miller et al.[1] and Da Silva et al.[3] demonstrated that convergence of both the interlayer relaxation and work function occurs with 6 layers for the Pt(111) surface to within 0.02 Å and 0.01 eV respectively. However, each study emphasizes care when calculating the surface energy. As these calculations use the bulk properties as a reference, one can introduce errors through inconsistencies in 1BZ sampling between the bulk and surface calculations.[6] However, one can drastically reduce errors by using i) a sufficiently dense **k**-point mesh (typically around 30x30x30 or more) across both calculations or ii) the method outlined by Fiorentini and Methfessel;[6] where the reference bulk energy is extracted from a set of successively thicker surfaces as opposed to a single bulk calculation.

One can also achieve adequate reciprocal space sampling by increasing the size of the simulation cell, which correspondingly reduces the volume of the 1BZ. For a sufficiently large simulation cell, the variation across the 1BZ decreases such that only one **k**-point (known as the Γ-point at **k**=0) is required to achieve convergence with respect to reciprocal space sampling. However, as the plane wave basis extends across the entire simulation cell, the memory requirement of the calculation increases dramatically with simulation cell size. This is especially punishing in slab supercell simulations, where large volumes of vacuum must be included in the system to avoid self-interaction between adjacent periodic images. Santarossa et al.[2] demonstrated the equivalence between the Γ-point and the Monkhorst-Pack sampling scheme for Pt(111) and Pt(110). Their study shows close agreement with the dense **k**-point approaches with (1x1) units cells, provided the bulk and surfaces are constructed with upwards of (6x6) repeating units of Pt. The memory

cost of vacuum was made more manageable using the Gaussian Plane Wave (GPW)[7] basis approach as implemented in the CP2K code, which represents the charge density of Gaussian basis functions through an auxiliary plane wave basis set. The DFT formalism implemented in the linear-scaling DFT code, ONETEP[8] presents another approach for reducing the vacuum cost. By representing the plane waves as a set of highly localized periodic sinc (psinc) basis functions which are used to expand atom-centered NGWFs strictly localized within spherical regions, unnecessary computations are avoided in vacuum regions of the simulation cell.

S2. Pt Bulk Properties

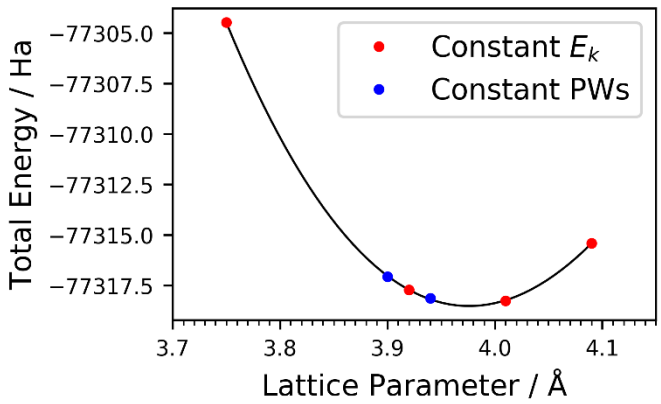

Figure S1: The Birch-Murnaghan fitting procedure is carried out for an 864 Pt atom simulation cell. The quality of the basis is kept constant for each of the blue markers and the number of *psinc* basis functions vary. Red markers show the psinc kinetic energy cut off E_k is varied by approximately 10 eV to the nearest adjacent while the number of psinc basis functions remains constant.

The bulk is constructed as a set of (6×6×6) FCC unit cells containing 864 Pt atoms, where the simulation cell volume is varied through a lattice constant of 3.75 to 4.09 Å. The Birch-Murnaghan equation of state[9] is then used to obtain the equilibrium lattice constant and bulk modulus. Variations in cell size require careful treatment to keep the underlying basis set description as invariant as possible. One can either i) fix the basis quality by keeping the kinetic energy cut-off E_k constant, but increasing the number of plane waves, as outlined by Skylaris et al.[10], or ii) fix the number of basis functions, but varying the value of E_k. Here we combine both approaches as shown in Figure S1.

Table S1: Bulk properties obtained with different DFT methods, all using the PBE functional. PW approaches shown use a (1×1) unit cell of the fcc bulk with (21×21×21) **k**-point sampling. Both ONETEP and the GPW calculations were performed with **Γ**-point only sampling, with a (6×6×6) unit cell.

Calculation Method	Bulk Modulus / GPa	Lattice Constant / Å
ONETEP (6×6×6 unit cell)	268	3.98
Plane Wave (1)[a]	246	3.99
GPW (6×6×6 unit cell)[b]	270	3.97
Plane Wave (2)[c]	241	3.97
Experimental Value[d]	278	3.92

a; Ref[1] b; Ref[2] c; Ref[3] d; Ref[11]

In ONETEP, E_k is inversely proportional to the square of the grid spacing of the underlying psinc functions. In order to keep the value of E_k constant, the psinc spacing must also remain unchanged.

This is done by varying the simulation cell size in discrete multiples of the underlying grid spacing (0.258 Å). An exception to this is the two points highlighted in blue in *Figure 1*. Here instead of keeping the psinc spacing constant and varying the number of grid points, we keep the number of grid points constant and vary the E_k by expanding the cell by a small amount (0.14 $Å^3$), with the number of plane waves kept constant. This only leads to an increase in psinc spacing of 0.0015 Å (or E_k ~10 eV). As we can see from Figure 1, the method of varying E_k produces far smaller fluctuations in total energy compared to the changes due to the lattice parameter, so we will take also these points into account in our calculation of the equilibrium lattice constant. The points shown in figure 1 correspond to lattice constants of 3.75 Å (with 87 grid points in each dimension), 3.90 Å (91 grid points with increased spacing), 3.92 Å (91 grid points), 3.94 Å (91 grid points with decreased spacing), 4.01 Å (93 grid points) and 4.09 Å (95 grid points). These points were selected as they are multiples of prime numbers and allow efficient FFTs for the calculation of the Hartree potential. The points with 89 grid points (3.83 Å) were not possible to use as they lead to very slow calculations as they are not divisible to smaller numbers of points for efficient FFTs.

Table S1 shows the values of the lattice constant obtained via the Birch-Murnanghan equation from our points in Figure 1 compared to PBE calculations with other methods such as the GPW Γ–point only approach used by Santarossa et al.[2] and plane wave approaches with k-point sampling. There is close agreement in the lattice constants between ONETEP (3.98 Å) and the other methods which produce values in the range 3.97-3.99 Å. We also quote the experimental value which is 3.92 Å – it is well known that PBE overestimates this lattice constant.[12] The values of the bulk modulus show a wider spread in the range 246-270 GPa with the PW results in the range 241-246 GPa and ONETEP 268 GPa being very close to the value of GPW which is 270

GPa and close to the experimental value of 278 GPa. The much closer agreement with experiment of the GPW and ONETEP calculations may be an artefact of the use of localized orbitals in these approaches.

S3. Surface Calculations in Vacuum

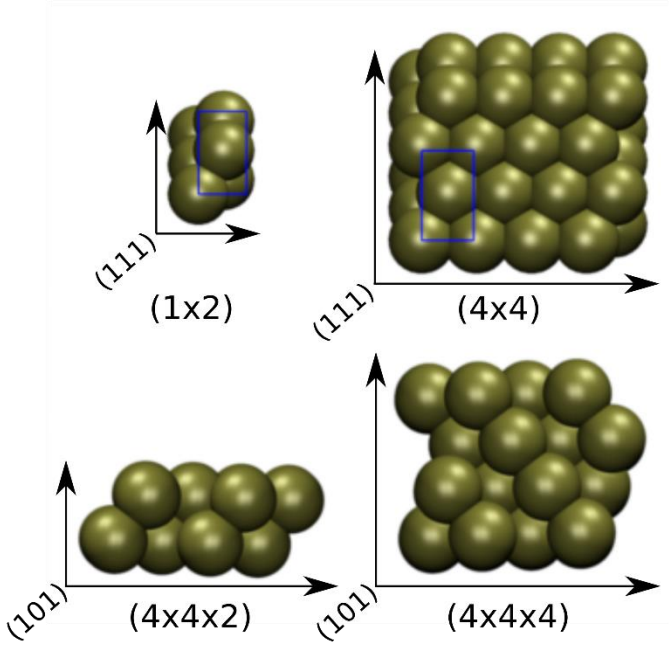

Figure S2: Illustrates the (4×4) supercell of the Pt(111) facet with its underlying (1×2) unit cell viewed through the z-axis (top panel, (111) facet) and its corresponding view through the y-axis (bottom panel, (101) facet) showing two cells of N=2 and N=4 thickness.

Surface calculations were performed with the periodic supercell method with a slab model. This approach emulates an infinitely extended metallic surface of a specified thickness through a set of repeated unit cells. To avoid self-interaction, the periodic images were separated by at least 20 Å of vacuum in the z-direction. Surfaces were constructed from sets of (1×2), orthorhombic unit

cells for Pt(111) (as shown in Figure S2). In order to test convergence with respect to **Γ**-point sampling, calculations were performed with a 5-layer slab with increasing numbers of unit cells in the x and y directions (ie. (4×4), (5×6), (6×6), (7×6) and (8×8). Energetic and structural properties were also evaluated with respect to the number of layers in the slab in order to validate our structures for use in solvation calculations. This was performed with the (7×6) surface slab.

S2.1 Work Function and Surface Energy

Table S2: Energetic properties for the Pt(7×6×N) set of slabs, including the work function and the surface energy, as calculated with the Fiorrentini method.[6]

Species	Vacuum Φ / eV	Surface Energy, σ / eV Å^{-2}
Pt(7×6×2)	5.72	0.69
Pt(7×6×3)	5.82	0.68
Pt(7×6×4)	5.70	0.66
Pt(7×6×5)	5.71	0.68
Pt(7×6×6)	5.64	0.68
Pt(7×6×7)	5.65	0.69
Pt(7×6×8)	5.64	0.68
PW[a]	5.69	0.65
Experiment	6.10 ± 0.06[b]	0.96[c]

[a] PW with 13-layer slab.[1] :[b] UHV LEED.[13] [c] Ref[14]

The work function (ϕ) represents the minimum energy required to remove an electron from the metallic surface to a location in the vacuum where the variation of the electrostatic (Hartree) potential is no longer influenced by the charge density of the metallic species. This work will

follow the convention where ϕ is calculated as the difference between the Fermi level E_F and the plane-averaged electrostatic potential V at a mid-point in the vacuum region between the Pt slab and its adjacent periodic:

$$\phi = E_{vac} - E_{F,} \quad \text{(S1)}$$

where E_{vac} is calculated as an average of the electrostatic potential in an xy-plane 10 Å above the surface.

For slabs with N=2 to N=5, the value of the work function fluctuates between 5.82 to 5.70 eV (Table S2). This implies finite size effects introduce significant errors to the work function for N<6. However, the work function values for N>6 converge within ±0.1 eV of the thickest surface slab. Furthermore, our converged value of 5.64 ± 0.1 eV compares favorably to the value of 5.61 ± 0.1 eV for the GAPW approach[2], and the 5.69 ± 0.05 eV value of the PW approach with multiple *k*-points.[1]

The surface energy of a metallic facet is defined as the free energy per unit area relative to the bulk for a particular crystal facet. In essence, this quantity describes the free energy of formation of a surface compared to the bulk crystal. The simplest way to calculate surface energy, σ, is through the expression:

$$\sigma = \frac{1}{2\,A}\left(E_{surf}^{N} - NE_{bulk}\right), \quad \text{(S2)}$$

where E_{surf}^{N} represents the total energy of the metallic surface of N Pt atoms, and E_{bulk} represents the energy of a single Pt atom within the bulk. Due to the symmetry of the slab, the surface energy per unit area can be obtained by a division of the total slab surface area, 2A. As mentioned in the introduction, the accuracy of σ is limited by the correspondence of **k**-point sampling of the surface and bulk calculations. The method of Fiorrenttini et al.[6] circumvents this

issue by obtaining E_{bulk} from as a linear regression of E_{surf}^{N} for a set of surface slabs of increasing numbers of layers N_{layer}, but with a constant number of constituent unit cells and **k**-points.

Applying this method to the Pt(7×6×N) surfaces, σ converges to a value of 0.68 ± 0.01 eV/Å^2 with 5 layers (Table S2), where the value continues to fluctuate marginally for the surface with 7 layers. These values are consistent with similar studies carried out with other PW methods. For example, our values are especially compatible with the 13-layer converged surface of *Singh-Miller et al.*,[1] where agreement was found within 0.02 eV/Å^2.

S3.2 Interlayer Spacing

The interlayer spacing (or interlayer relaxation) describes the change in distance between each of the metallic layers relative to the unrelaxed surface (in the bulk positions):

$$\Delta d_{ij}\ \% = \frac{d_{ij}^{relaxed} - d^{unrelaxed}}{d^{relaxed}} \times 100\ \%, \quad \text{(S3)}$$

where $d_{ij}^{relaxed}$ is the distance between layers i and j and $d_{ij}^{unrelaxed}$ is taken as $a_0/\sqrt{3}$ (along the (111) direction of a FCC metal), where a_o is the equilibrium bulk lattice constant. Throughout the paper, a positive value of Δd_{ij} % corresponds to an expansion and a negative to a compression of the surface slab relative to the unrelaxed structure.

Previous benchmark studies by Singh-Miller et al. using the PWSCF method[1] found that the interlayer spacing for the first layer Pt(111) expands by ~1.0%, while the second layer contracts ~0.5 % relative to the bulk value.

Although convergence with respect to the numbers of unit cells was achieved with Pt(7×6×5), the magnitude of Δd_{12} % is smaller than Δd_{23} % for both of these surfaces. This is quantitatively inconsistent with the results of previous benchmark studies, but this is shown to be an artefact of finite size effects, as shown by the increasing the number of layers of the Pt(7×6×N) slab from

N=2 to N=9 (Table S3). For slabs N < 6, the interlayer spacing fluctuates significantly from the N=9, with Δd_{23} and Δd_{12} varying by up to 0.032 Å. Although the qualitative expansion of Δd_{12} and contraction of Δd_{23} are observed for N=4 to N=6, the magnitude of Δd_{23} % for these thicknesses are relatively larger than Δd_{23} % for N > 6. This is quantitatively inconsistent with interlayer spacing changes for N=9 and the thickest slabs of the PW and GPW approaches, where Δd_{23} % contractions are consistently 0.3-0.5% smaller than the expansions of the first and second layer.

Table S3: Interlayer spacing after full geometry relaxation for a set of increasingly thicker Pt(111) slabs from 2 to 9 layers. These values are compared against **Γ**-point only calculations with GPW (Quickstep), and a PW (PWSCF) calculation with an (8×8) Monkhorst-Pack grid and 13 Pt layers.

Slab Dimensions	Δd_{12} /Å	Δd_{23} /Å	Δd_{12} %	Δd_{23} %
Pt(7×6×2)	2.310	-	0.69	-
Pt(7×6×3)	2.290	2.290	-0.18	-0.18
Pt(7×6×4)	2.313	2.240	0.82	-2.36
Pt(7×6×5)	2.304	2.274	0.43	-0.88
Pt(7×6×6)	2.312	2.272	0.77	-0.97
Pt(7×6×7)	2.313	2.281	0.82	-0.58
Pt(7×6×8)	2.314	2.284	0.86	-0.45
Pt(7×6×9)	2.317	2.280	0.99	-0.62
Pt(8×8×8)[a]	2.315	2.278	1.13	-0.49
PW 13-layers[b]	-	-	0.85	-0.56

a: GPW[2] ; b: Converged PW study with 13 layers[1]

However, interlayer spacing changes converge with slab thicknesses $N \geq 7$, where the maximum fluctuation in Δd_{12} and Δd_{23} is small (0.003 Å). Also of note is the similarity between our results and those of the GPW **Γ**-point only approach. Here, we see the differences for the Δd_{12} between the Pt(8×8×8) and Pt(7×6×9) surfaces are 0.001 Å, and 0.006 Å for Δd_{23}, respectively. We conclude that a surface slab such as Pt(7×6×7) with the **Γ**-point approach is sufficiently large to provide geometric relaxation parameters comparable with a conventional calculation of a small cell with extensive k-point sampling.

S4. k-point Convergence of Pt(111)

Table S4: The convergence of the work function for slabs with increasing size in the xy-plane to demonstrate convergence is achieved in the **Γ**-point approximation.

Slab Dimension	Work Function ϕ / eV
Pt(4×4×5)	5.65
Pt(5×6×5)	5.66
Pt(6×6×5)	5.66
Pt(7×6×5)	5.70
Pt(8×8×5)	5.68

We performed additional convergence tests with respect to Brillouin Zone sampling by using increasingly large supercells in the xy-direction. Here, we demonstrate that the value of the work function shows relatively small variation from Pt(4×4×5) to Pt(8×8×5), showing a difference of 0.03 eV between the smallest and the largest slabs (Table S4).

Conversely, the interlayer spacing is more sensitive to BZ sampling. Compared to the converged Pt slab, the smaller systems (Pt(5×6) and Pt(6×6)) exhibit a large contraction of the second layer while the expansion of the first layer tends to be smaller (with the exception of Pt(4×4)). For slabs larger than Pt(7×6), the geometry converges to within 0.01 Å (Table S5).

Table S5: The convergence of interlayer spacing for a 5 layer Pt slab with increasing size in the xy-plane to demonstrate convergence is achieved in the **Γ**-point approximation.

Slab Dimensions	Δd_{12} /Å	Δd_{23} / Å	Δd_{12} %	Δd_{23} %
Pt(4×4×5)	2.330	2.291	1.63	-0.03
Pt(5×6×5)	2.297	2.244	0.21	-2.10
Pt(6×6×5)	2.292	2.252	-0.01	-1.78
Pt(7×6×5)	2.304	2.274	0.43	-0.88
Pt(8×8×5)	2.302	2.263	0.42	-1.30
Pt(8×8×5)[a]	3.202	2.268	0.59	-0.93
PW 13-layers[b]	-	-	0.85	-0.56

a: GPW[1] ; b: Converged PW study with 13 layers[2]

S5. Soft Sphere and Isodensity Pt(111) Interfaces

Both soft sphere and isodensity cavitation models can replicate the overall charge displacement of the equilibrated AIMD simulation of the Pt/(H_2O) interface. The two cavitation models produce

subtly different shapes of the dielectric function (Figure S3), where the soft sphere approach produces a less planar topology than the isodensity method.

The differences in the electronic structure induced by the soft sphere and isodensity models are relatively minor. Figure S4 shows the d-projected DOS and DOS difference plots of the two cavitation models. Here, we observed the two d-bands exhibit broadly similar changes between -2 to -6 eV, with slightly more pronounced changes near the Fermi level. These changes likely arise from the different topologies of the dielectric cavities, leading to differing electronic structure changes.

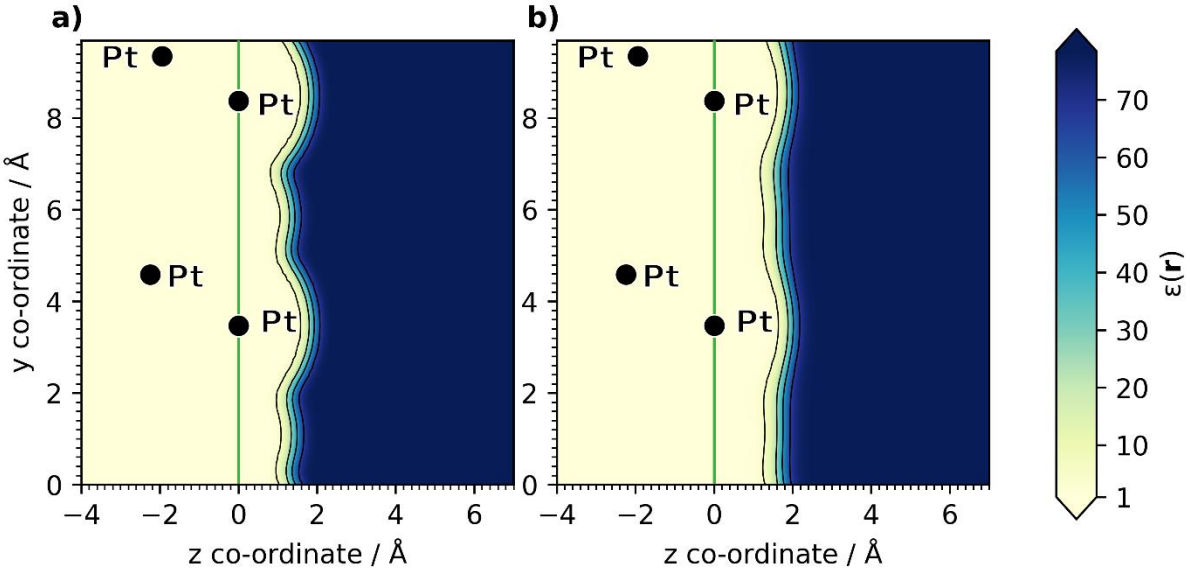

Figure S3: Dielectric permittivity across an xy-slice of the Pt(111) surface for: a) the soft sphere cavitation model and b) the isodensity model.

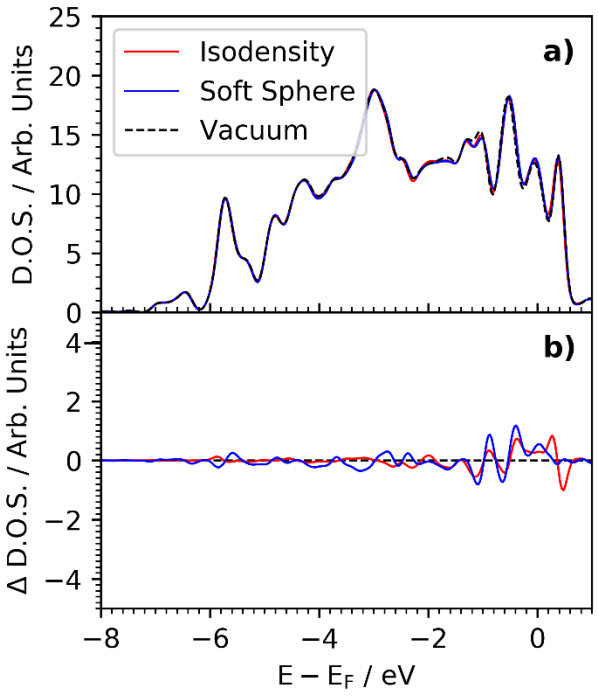

Figure S4: a) Projected Density of States (PDOS) of the surface Pt atoms, projected into the d-band, averaged across 90 AIMD snapshots for the Pt(4x4x4) in vacuum and Pt(4x4x4)/continuum interface with the soft sphere and isodensity model. Energies relative to the Fermi level, E_F. b) Difference of the PDOS d-band with respect to the Pt surface in vacuum.

S6. Water distribution from AIMD

Water distribution along the surface normal direction is given by

$$\rho(z) = \frac{\langle n(z) \rangle}{d\,V} m, \qquad \text{(S2)}$$

where $\frac{\langle n(z) \rangle}{d\,V}$ is the average number of water molecules in the volume dV between two planes parallel to the surface located at z and z+dz, and m is the mass of a water molecule.

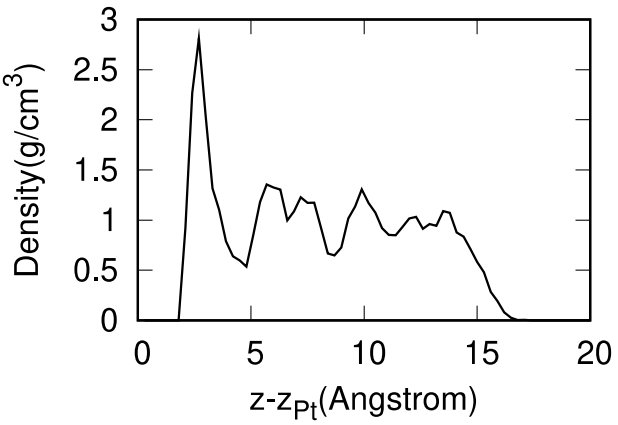

Figure S5: Water density as a function of distance to the Pt surface.

S6. Water Rotation Dynamics

The rotation of water molecules directly affects the net dipole moment of the water layer at the interface. To understand the rotational dynamics of water we computed the auto-correlation function of dipole moments of water molecules in the interfacial layer (the first layer, see Figure S5).

The auto correlation function is given by:

$$C(t) = \frac{\langle \boldsymbol{\mu}(0)\boldsymbol{\mu}(t)\rangle}{\langle \boldsymbol{\mu}(0)\boldsymbol{\mu}(0)\rangle} \quad \text{(S3)}$$

in which $\boldsymbol{\mu}$ is the dipole vector moment of a water molecule and the notation < > implies the ensemble average. Only water molecules that stay continuously in the interfacial layer were considered. Thus, we split the whole AIMD trajectory into 3 smaller trajectories (8 ps each). Finally, C(t) was averaged over the three trajectories.

The long-time behavior of C(t) is indicated in Figure S4. We use this part of the auto-correlation function and obtain the characteristic time constant t* by fitting the numerical data with the $a.e^{-t/t^*}$ function.

It appears that t* is approximately 10.7 ps which indicates that our trajectories of 24 ps should be enough capture the rotational contribution of water to the net dipole moment.

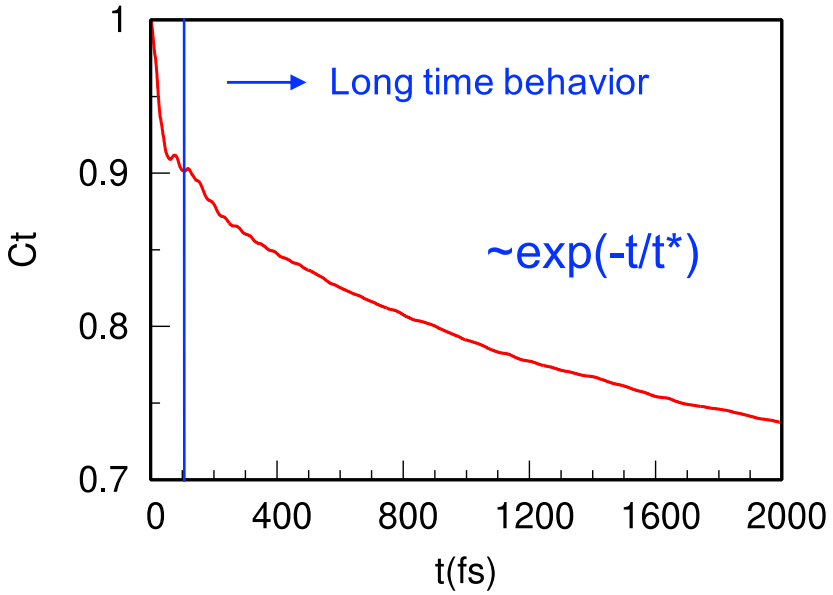

Figure S6: Auto-correlation function of water dipole moments. Only water molecules in the double layer were considered. The long time behavior is indicated.

S7. Water exchange rate

To see if there are enough events for the water exchange process between the interfacial layer and the rest of the water film we estimated the rate of this process. According to Chandler[15], the rate can be determined by the following procedure. Briefly, for each water molecule we can define at population function *h*, which is 1 if the water is in the interfacial layer and 0 otherwise. Next, we compute the instantaneous population fluctuation

$$\delta h(t) = h(t) - \langle h \rangle \quad \text{(S4)}$$

$\langle h \rangle$ is the time average of h, and essentially, it tells us the amount of time spent in the interfacial layer. The rate constant for water molecules to enter and leave this layer, k, can be estimated from

$$-\frac{d}{dt}\left(\frac{\langle h\delta h(t)\rangle}{\langle h\delta h\rangle}\right) \sim k\, e^{-k.t} \quad \text{(S5)}$$

The left and right sides of eqn S5 from our simulation are shown in Figure S7. k is estimated to be 4 event/ps

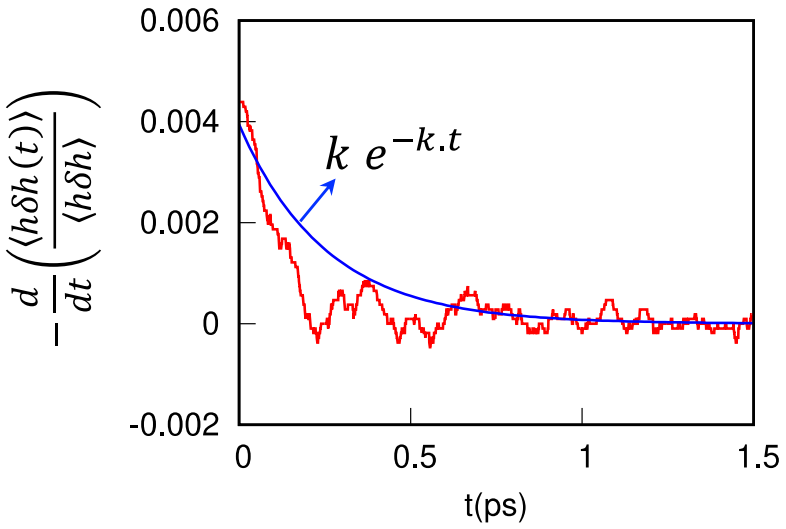

Figure S7: The left and right sides of eqn S5 for our system from AIMD.

S8. Approximating ΔH_{solv} for Pt(111)

In the bond additivity scheme of Singh and Campbell[16], solvation can be envisioned as a process of bond breaking between the water-water interface (W-W) and formation of water-adsorbate bonds (W-A),

$\Delta H_{solv} = \text{W-W} - 2(\text{W-A})$, (S6)

(See Scheme 2 of ref.[16]). This scheme envisions a column of water with the cross-sectional area of the adsorbate. The uphill energetics of breaking the W-W bond is taken as the twice surface energy of water for the area of the adsorbate (W-W = $2\gamma_{water(liquid)}$ = 0.146 Jm^{-2})[17]. W-A is taken as the bond energy between Pt(111) and water, which is taken as the adhesion energy of liquid water with the Pt surface ($E_{adh,W(liq)/Pt}$), however, in the Campbell scheme, the adhesion energy is approximately calculated using the energetics for a film of solid water ($E_{adh,W(s)/Pt}$). Using eq. S6, the approximations applied to phenol can be extended to the Pt(111) surface. Knowing both $E_{adh,W(s)/Pt}$ = 116 $kJmol^{-1}$ (see ref[16]) and $2\gamma_{water(liquid)}$ = 52.7 $kJmol^{-1}$ for the footprint area of phenol, and phenol occupies 9 Pt atoms upon adsorption, we can approximate the heat of solvation for a single Pt atom as follows:

$$\Delta H_{solv} = (2\gamma_{water(liquid)})/36 - (2E_{adh,W(s)/Pt})/36$$
$$= \frac{52.7\ kJmol^{-1} - 232\ kJmol^{-1}}{18}$$
$$= -9.61\ kJmol^{-1}, \text{ (S7)}$$

S9. Enthalpy Changes of Solvation

Table S6 gives a breakdown of the values involved in the Hess cycle used in Scheme 1. We further note the values of $\frac{\text{area of phenol cavity}}{\text{area of Pt surface}}$ used in the calculation of $-\Delta H^{slab}_{desolv}$, where the proportion of cavity coverage for soft sphere and isodensity with PBE/rVV10 are 25%/25% and 21%/20% respectively.

Table S6: Enthalpy changes outlined in Scheme 1 for the adsorption of phenol to the Pt(111) (Pt(6x6x4)) facet under aqueous conditions. Calculations were performed with the re-fitted cavity parameters obtained in Section 3.4 for both soft sphere and isodensity methods. Solvation enthalpies ΔH^{int}_{solv} and $\Delta H^{non-int}_{solv}$ include the solvation of the whole Pt surface. $\Delta H^{phenol+slab}_{desolv}$

shows the enthalpy change associated with the desolvation of the slab and phenol upon adsorption. ΔH_{ads}^{aq} corresponds to the heat of adsorption under aqueous conditions. All values in kJ mol^{-1}.

Cavitation Model	ΔH_{ads}^{vac}	$\Delta H_{ads,desolv}$	$\Delta H_{solv}^{non-int}$	ΔH_{solv}^{int}	$\Delta H_{desolv}^{phenol+slab}$	ΔH_{ads}^{aq}
PBE (Isodensity)	-122.88	36.88	-727.53	-1041.41	-317.36	-280.49
PBE (Soft Sphere)		29.09	-1004.87	-357.43	-134.03	-104.94
VV10 (Isodensity)	-188.69	-48.50	-539.11	-892.95	-269.88	-318.38
VV10 (Soft Sphere)		-35.51	-1040.20	-378.86	-141.42	-176.93
Bond-Additivity Model[16]	- 200.0[18,b]	-	-	~ -21.0[19,a]	~ -116.0	-148.4[a]/ ~ -200.0[b]

1. Singh-Miller, N. E.; Marzari, N., Surface energies, work functions, and surface relaxations of low-index metallic surfaces from first principles. *Phys. Rev. B* **2009,** *80*.
2. Santarossa, G.; Vargas, A.; Iannuzzi, M.; Pignedoli, C. A.; Passerone, D.; Baiker, A., Modeling bulk and surface Pt using the "Gaussian and plane wave" density functional theory formalism: Validation and comparison to k-point plane wave calculations. *J. Chem. Phys.* **2008,** *129*.
3. Da Silva, J. L. F.; Stampfl, C.; Scheffler, M., Converged properties of clean metal surfaces by all-electron first-principles calculations. *Surf. Sci.* **2006,** *600*, 703-715.
4. Clark, S. J.; Segall, M. D.; Pickard, C. J.; Hasnip, P. J.; Probert, M. J.; Refson, K.; Payne, M. C., First principles methods using CASTEP. *Z. Phys. Chem.* **2005,** *220*, 567-570.
5. Monkhorst, H. J.; Pack, J. D., Special Points for Brillouin-Zone Integrations. *Phys. Rev. B* **1976,** *13*, 5188-5192.
6. Fiorentini, V.; Methfessel, M., Extracting convergent surface energies from slab calculations. *J. Phys. Condens. Matter* **1996,** *8*, 6525-6529.
7. Lippert, G.; Hutter, J.; Parrinello, M., A hybrid Gaussian and plane wave density functional scheme. *Mol. Phys.* **1997,** *92*, 477-487.
8. Skylaris, C. K.; Haynes, P. D.; Mostofi, A. A.; Payne, M. C., Introducing ONETEP: Linear-scaling Density Functional Simulations on Parallel Computers. *J. Chem. Phys.* **2005,** *122*, 084119.
9. Birch, F., Finite Elastic Strain of Cubic Crystals. *Phys. Rev.* **1947,** *71*, 809-824.

10. Skylaris, C. K.; Haynes, P. D., Achieving plane wave accuracy in linear-scaling density functional theory applied to periodic systems: A case study on crystalline silicon. *J. Chem. Phys.* **2007,** *127*.
11. Kittel, C., *Introduction to Solid State Physics*. Wiley 2005.
12. Hammer, B.; Hansen, L. B.; Norskov, J. K., Improved adsorption energetics within density-functional theory using revised Perdew-Burke-Ernzerhof functionals. *Phys. Rev. B* **1999,** *59*, 7413-7421.
13. Derry, G. N.; Zhang, J. Z., Work Function of Pt(111). *Phys. Rev. B* **1989,** *39*, 1940-1941.
14. Kumikov, V. K.; Khokonov, K. B., On the Measurement of Surface Free-Energy and Surface-Tension of Solid Metals. *J. Appl. Phys.* **1983,** *54*, 1346-1350.
15. Chandler, D., Barrier crossings: classical theory of rare but important events. In *Classical and Quantum Dynamics in Condensed Phase Simulations*, B. J. Berne, G. C. a. D. F. C., Ed. World Scientific: Singapore, 1998; p 3.
16. Singh, N.; Campbell, C. T., A Simple Bond-Additivity Model Explains Large Decreases in Heats of Adsorption in Solvents Versus Gas Phase: A Case Study with Phenol on Pt(111) in Water. *ACS Catal.* **2019,** *9*, 8116-8127.
17. In *Intermolecular and Surface Forces (Third Edition)*, Israelachvili, J. N., Ed. Academic Press: San Diego, 2011; pp 635-660.
18. Carey, S. J.; Zhao, W.; Mao, Z.; Campbell, C. T., Energetics of Adsorbed Phenol on Ni(111) and Pt(111) by Calorimetry. *The Journal of Physical Chemistry C* **2019,** *123*, 7627-7632.
19. Singh, N.; Sanyal, U.; Fulton, J. L.; Gutiérrez, O. Y.; Lercher, J. A.; Campbell, C. T., Quantifying Adsorption of Organic Molecules on Platinum in Aqueous Phase by Hydrogen Site Blocking and in Situ X-ray Absorption Spectroscopy. *ACS Catal.* **2019,** *9*, 6869-6881.